Supplemental Information

Why Enveloped Viruses Need Cores—The Contribution of a Nucleocapsid Core to Viral Budding

Guillermo R. Lázaro, Suchetana Mukhopadhyay, and Michael F. Hagan

SUPPLEMENTAL INFORMATION

S1. SIMULATION MOVIES

- **Simulation Movie 1.** Animation of a typical simulation showing GP-directed budding, for $\epsilon_{gg} = 2.5$ and $\kappa_{mem} = 14.5 k_{B}T$. Colors are as follows: GPs, magenta; membrane head groups, cyan; membrane tails, yellow. To show the membrane neck geometry more clearly the inactive subunits are rendered invisible in this animation.

- **Simulation Movie 2.** The same simulation trajectory as in Simulation Movie 1, but rendered to show a central cross-section of the budding shell and the membrane. Inactive subunits are rendered brown in this animation.

- **Simulation Movie 3.** Animation of a typical simulation showing NC-directed budding, for $\epsilon_{gg} = 2.5$, $\epsilon_{ng} = 3.5$, and $\kappa_{mem} = 14.5 k_{B}T$. Colors are as in Simulation Movie 1, and the NC is colored blue. To show the membrane neck geometry more clearly we do not show inactive subunits in this animation.

- **Simulation Movie 4.** Animation showing a central cross-section of the NC-directed budding (same simulation trajectory as in Simulation Movie 3). Inactive subunits are shown in brown in this animation.

S2. EQUILIBRIUM MODEL FOR THE DEPENDENCE OF GP SHELL SIZE ON SYSTEM PARAMETERS

In this section we give a detailed derivation of Eq. 1 of the main text. This expression explains the simulation results for GP shell size as a function of control parameters (Fig. 6), and is obtained from a simple equilibrium model based on the thermodynamics of assembly [1, 2] that accounts for the elasticity of the shell and the membrane.

The total free energy for the system of free subunits on the membrane, shell intermediates of size n, and complete shells of size N can be expressed as

$$F/k_{B}T = \sum_{n=1}^{N} \rho_n [\log \rho_n v_0 - 1] + \rho_n G_n^{shell}/k_{B}T, \tag{S1}$$

where ρ_n and G_n^{shell} are respectively the concentration and interaction free energy for an intermediate with size n, and v_0 is a standard state volume. Minimization of Eq. (S1) subject to the constraint of constant subunit concentration yields the well-known law of mass action for the equilibrium distribution of intermediate concentrations,

$$\rho_n v_0 = \exp\left[-\left(G_n^{shell} - n\mu_1 \right)/k_{B}T \right]. \tag{S2}$$

with

$$\mu_1 = \log \rho_1 v_0 \tag{S3}$$

the chemical potential of free subunits. Similarly we can compute the chemical potential for intermediates $\mu = \partial F/\partial \rho_n$ as

$$\mu_n = \log \rho_n v_0 + G_n^{shell}/k_{B}T. \tag{S4}$$

Note that to simplify the calculation we are assuming that the membrane spontaneous curvature is zero everywhere and that the membrane bending modulus is uniform in space; i.e., we are neglecting the influence of membrane domains. Many enveloped viruses preferentially bud from certain domains [3–5], and modeling suggests several mechanisms by membrane microdomains can promote assembly and budding [6]. We also neglect the role of transient clusters of subunits which may form due to sensing of local membrane curvature [7], although this would just shift the chemical potential of free subunits.

For large shells, the first term in (S4) is neglegible compared to the free energy of the shell, and the chemical pontential can be approximated as $\mu_n \approx G_n^{shell}/k_{B}T$. In equilibrium, the chemical potential of free subunits must be equal to that of subunits in shells and intermediates, leading to $\mu_1 = \mu_n/n \approx G_n^{shell}/n k_{B}T$.

The intermediate size with maximal concentration is determined by the condition

$$\frac{d\rho_n}{dn} = \rho_n \frac{d}{dn}[-G_n^{shell} k_{B}T + n\mu_1] = 0, \tag{S5}$$

which using (S3) and (S4) can be rewriten as

$$\frac{d}{dn}[-G_n^{shell}/k_{B}T + n\mu_1] \approx \left[-\frac{dG_n^{shell}}{dn} + G_n^{shell}/n \right]/k_{B}T. \tag{S6}$$

Thus, the optimal size at equilibrium is that which minimizes the interaction free energy per subunit, G_n^{shell}/n.

The interaction free energy includes subunit-subunit interactions and the elastic energy of the shell and the membrane. Assuming that the shell can be described as a continuous, two-dimensional spherical shell, its elastic energy is given by the Helfrich bending energy, with bending modulus κ_{shell} and spontaneous curvature $c_0 = 2/R_0$, where R_0 is the equilibrium radius of the shell. The membrane underneath is a symmetric bilayer with rigidity κ_{mem}. The free energy G_n^{shell} thus reads

$$G_n^{\text{shell}} = n\Delta g_{\text{g}} + \frac{\kappa_{\text{mem}}}{2} \int_S c^2 dS + \frac{\kappa_{\text{shell}}}{2} \int_S (c - c_0)^2 dS, \tag{S7}$$

where Δg_{g} is the free energy per subunit added to the shell, c is the total curvature, and S denotes the surface area. Assuming spherical symmetry and accounting for the fact that the subunits are rigid, the shell surface area is $S \approx nS_0$, with S_0 as the area per subunit. We can then express the total curvature as a function of the number of subunits in the particle, $c = 2/R \approx (16\pi/nA_0)^{1/2}$. Here we are assuming that the Gaussian modulus of the membrane is unchanged by the presence of the GPs, so that the integrated Gaussian curvature is constant for fixed topology by the Gauss-Bonnet theorem [8]. Under the (reasonable) assumption that the shell size is determined before scission, the Gaussian curvature energy then contributes a constant to the free energy and can be neglected. We have neglected the energy from the 12 disclinations in the shell. Accounting for this could shift the theory curve in Fig. 6b but would not change the slope. We also neglect the logarithmic dependence of the effective bending rigidity on the bud size [9], since including this effect changes the optimal size by less than 2%.

Finally, recalling that the equilibrium configuration minimizes the interaction free energy per subunit, G_n^{shell}/n results in (1) of the main text,

$$n = n_0 \left(1 + \frac{\kappa_{\text{mem}}}{\kappa_{\text{shell}}}\right)^2, \tag{S8}$$

where n_0 is the number of subunits in the equilibrium configuration in the absence of membrane, corresponding to $n_0 = 80$ in our model.

S3. MODEL DESCRIPTION

This section gives complete details for the computational model. We begin with an overview of each component of the model, and then give the full set of interaction potentials in section S3 G.

A. Glycoproteins and capsid

Our coarse-grained GP model is motivated by the geometry of Sindbis virions as revealed by cryoelectron microscopy [10, 11]. The outer layer of Sindbis is comprised from heterodimers of the E1 and E2 GPs. Three such heterodimers form a tightly interwoven trimer-of-heterodimers, and 80 of these trimers are organized into a T=4 lattice. On the capsid surface each trimer forms a roughly equilateral triangle with edge-length $\sim$ 8nm. In the radial direction, each E1-E2 heterodimer spans the entire lipid membrane and the ectodomain spike, totaling $\sim$ 12nm in length. In our model, we consider the GP trimer as the basic assembly subunit, assuming that the formation of trimers is fast relative to the timescale for assembly of trimers into a complete capsid. Our subunit model aims to capture the triangular shape, aspect ratio, and preferred curvature of the GP trimers while minimizing computational detail as described in the main text. The cone length and trimer organization within the capsid are consistent with the Sindbis structure (see section S3 H for full details). Note that while the domains primarily responsible for curvature of alphavirus GPs are located to the exterior of the envelope, the conical regions which drive curvature of the model subunit oligomers are located within and below the plane of the membrane. We found that this arrangement facilitated completion of assembly (see a detailed explanation in section S3 H).

We set the preferred angle so that in bulk simulations (in the absence of membrane) the subunits predominantly assemble into aggregates with the target size, 80 subunits. However, there is a small amount of polydispersity, with some capsids having sizes between 79 and 82 subunits (Fig. S4) (discussed below in section S5).

B. Lipid membrane

The lipid membrane is represented by the implicit solvent model from Cooke and Deserno [12]. This model enables on computationally accessible timescales the formation and reshaping of bilayers with physical properties such as rigidity, fluidity, and diffusivity that can be tuned across the range of biologically relevant values. Each lipid is modeled by a linear polymer of three beads connected by FENE bonds; one bead accounts for the lipid head and two beads for the lipid tail. An attractive

potential between the tail beads represents the hydrophobic forces that drive lipid self-assembly. In section S6 we estimate the bending rigidity of the membrane in our simulations by analyzing their fluctuation spectra. Unless otherwise specified, our simulations used $\kappa_{\mathrm{mem}} \approx 14.5 k_{\mathrm{B}}T$ as a typical rigidity of plasma membranes.

C. Glycoprotein-membrane interactions

The effect of individual GPs on the behavior of the surrounding membrane has not been well characterized. Moreover, to facilitate interpretation of our simulation results, we require a model in which we could independently vary subunit-subunit interactions and subunit-membrane interactions. Therefore, we use the following minimal model for the GP-membrane interaction. We add six membrane excluder beads to our subunit, three at the top and three at the bottom of the subunit, with top and bottom beads separated by 7nm (Fig. 2c,d). These excluder beads interact through a repulsive Lennard-Jones potential with all membrane beads, whereas all the other cone beads do not interact with the membrane pseudoatoms. In a simulation, the subunits are initialized with membrane located between the top and bottom layer of excluders. The excluded volume interactions thus trap the subunits in the membrane throughout the length of the simulation, but allow them to tilt and diffuse laterally. Separating the subunit pseudoatoms that interact with the membrane from those which control the subunit-subunit potential allows us to independently vary subunit-subunit and subunit-membrane interactions. The position of the subunit-subunit interaction beads (cones) relative to the membrane excluders has little effect on the initial stages of assembly and budding, but strongly affects its completion (described in detail in section S3 H).

We note that the model does not account for local distortions within the lipid hydrophobic tails in the vicinity of the GPs. Such interactions could drive local membrane curvature and membrane-mediated subunit interactions which could either enhance or inhibit assembly and budding. Understanding these interactions is an active area (e.g. Refs. [13–17]) but beyond the scope of the present study.

D. Nucleocapsid

The NC is represented in our model by a rigid spherical particle. This minimal representation is based on two experimental observations. We model it as spherically symmetric because asymmetric reconstructions by Wang et al. [18] showed that the alphavirus NC does not exhibit icosahedral symmetry in virions (assembled in host cells) or viruslike particles (assembled in vitro). Second, within the NC-directed hypothesis the NC assembles completely in the endoplasmic reticulum and is then transported by the secretory pathway to the budding site at the plasma membrane. The complete NC has been shown to have a significantly higher rigidity than lipid membrane or GP-coated vesicles [19, 20]; thus, we model it as infinitely rigid.

Our model NC is constructed from 623 beads distributed on a spherical surface with radius $r_{\mathrm{NC}} = 19.0\sigma$, and subjected to a rigid body constraint. To represent the hydrophobic interactions between GPs cytoplasmic tails and the capsid proteins, NC beads and the third bead of the GP subunits (counting outwards) experience an attractive Morse potential, with well-depth ϵ_{ng}. The radius of the NC sphere was tuned using bulk simulations to be commensurate with a capsid comprising 80 GPs. To minimize the number of parameters, we do not consider an attractive interaction between the NC and membrane, but the NC beads experience a repulsive Lennard-Jones potential with all membrane beads.

E. GP Conformational changes and implementation of constant GP concentration

Experiments on several viral families suggest that viral proteins interconvert between 'assembly-active' and 'assembly-inactive' conformations, which are respectively compatible or incompatible with assembly into the virion [21–23]. Computational modeling suggests that such conformational dynamics can suppress kinetic traps [24, 25]. Conformational changes of the alphavirus GPs E1 and E2 are required for dimerization in the cytoplasm, and it has been proposed that the GPs interconvert between assembly-inactive and assembly-active conformations [23], possibly triggered by interaction with NC proteins [26]. Based on these considerations, our GP model includes interconversion between assembly-active and assembly-inactive conformations. The two conformations have identical geometries, but only assembly-active conformations experience attractive interactions to neighboring subunits. We adopt the 'Induced-Fit' model of Ref. [24], meaning that interaction with an assembling GP shell or the NC favors the assembly-active conformation. For simplicity, we consider the limit of infinite activation energy. In particular, with a periodicity of τ_{c} all the inactive subunits found within a distance 1.0σ of the capsid are switched to the active conformation, while any active subunits further than this distance from an assembling shell convert to the inactive conformation. Results were unchanged when we performed simulations at finite activation energies larger than $4k_{\mathrm{B}}T$.

In simulations performed at a constant total number of GPs the assembly rate progressively slows over the course of the simulation due to the depletion of unassembled subunits. This is an unphysical result arising from the necessarily finite size of

our simulations. Moreover, during an infection additional GPs would be targeted to and inserted into the membrane via non-equilibrium process (powered by ATP). Therefore, our simulations are performed at constant subunit concentration within the membrane (outside of the region where an assembling shell is located). To achieve this, we include a third subunit type called 'reservoir subunits', which effectively acts as a reservoir of inactive subunits. These subunits interact with membrane beads but experience no interactions with the other two types of GP subunits. With a periodicity of τ_c, reservoir subunits located in a local region free of active or inactive subunits (corresponding to a circumference of radius 1.5 times the radius of the largest subunit bead) are switched to the assembly-inactive state.

F. Simulations

We performed simulations in HOOMD-blue[27], version 1.3.1, which uses GPUs to accelerate molecular simulations. Both the subunits and the NC were simulated using the Brownian dynamics algorithm for rigid bodies. The membrane dynamics was integrated using the NPT algorithm, a modified implementation of the Martina-Tobias-Klein thermostat-barostat. The box size changes in the membrane plane, to allow membrane relaxation and maintain a constant lateral pressure. The out-of-plane dimension was fixed at 200σ.

Our simulated equations of motion do not account for hydrodynamic coupling between the membrane and the implicit solvent, which can accelerate the propagation of bilayer perturbations. To assess the significance of this effect, we performed an additional series of simulations which did account for hydrodynamic coupling, by evolving membrane dynamics according to the NPH algorithm in combination with a dissipative particle dynamics (DPD) thermostat. As expected from Matthews and Likos [28], we found that hydrodynamic interactions did enhance the rate of membrane deformations; however, budding proceeded only 1.1-1.2 times faster than with the NPT scheme. Moreover, the end-product distribution was the same with and without hydrodynamic interactions. Therefore, to avoid the increased computational cost associated with the DPD algorithm, we performed all subsequent simulations with the NPT method. The very limited effect of hydrodynamics can be understood from the fact that assembly timescales in our simulations are more strongly governed by subunit diffusion than by membrane dynamics (Fig. 7).

Our system size was constrained by the capsid dimensions and the need to access long timescales. Taking the Sindbis virion as a reference structure, the bilayer neutral surface radius in the virion is ≈ 24nm [11], so the surface area of the membrane envelope is $A_0 \sim 7200$nm^2. We thus needed to simulate membrane patches that were significantly larger than A_0 to ensure that the membrane tension remained close to zero and that finite-size effects were negligible. Throughout this manuscript we report results from simulations on a membrane patch with size 170×170nm^2 ($A \sim 28,900$nm^2), which contains $51,842$ lipids. We compared membrane deformations, capsid size and organization from these simulations against a set of simulations on a larger membrane (210×210nm^2, $A \sim 44,100$nm^2) and observed no significant differences, suggesting that finite size effects were minimal. Simulations were initialized with 160 subunits uniformly distributed on the membrane, including 4 active-binding subunits (located at the center of the membrane) with the remainder in the assembly-inactive conformation. In addition, there were 156 subunits in the reservoir conformation uniformly distributed. This relatively high GP concentration was based on the observation of high densities of glycoproteins in the membranes of cells infected with Sindbis virus [29]. Simulations performed at lower subunit concentrations led to slower assembly. We would expect a lower subunit concentration to shift the transition interaction strengths (ϵ_{gg}) to higher values, but we did not explore the effect of GP concentration on the phase diagram in detail.

The membrane was then equilibrated to relax any unphysical effects from subunit placement by integrating the dynamics for 1,500 τ_0 without attractive interactions between GPs. Simulations were then performed for 4,200 τ_0 with all interactions turned on. The timestep was set to $\Delta t = 0.0015$, and the thermostat and barostat coupling constants were $\tau_T = 0.4$ and $\tau_P = 0.5$, respectively. Since the tension within the cell membrane during alphavirus budding is unknown, we set the reference pressure to $P_0 = 0$ to simulate a tensionless membrane. The conformational switching timescale was set to $\tau_c = 3\tau_0$, sufficiently frequent that the dynamics are insensitive to changes in this parameter. When a nucleocapsid was present, we placed it in the center of the XY plane, 7nm below the membrane. This initialization was chosen because within the NC-directed hypothesis the NC assembles completely in the endoplasmic reticulum and is then transported by the secretory pathway to the budding site at the plasma membrane. To understand the effect the initial NC location, we performed some additional simulations with the NC placed further from the membrane. In most of these simulations the NC diffused away without interacting with the membrane. In such cases, the assembly outcomes are the same as in Fig. 4. However, in a few simulations with sufficiently large ϵ_{gg} for the GPs to assemble without the NC, the NC eventually bound to the growing capsid, leading to an assembly outcome similar to the 'partially attached' structure shown in Fig. 5. Unless otherwise specified, for each parameter set we performed 8 independent simulations.

G. Interaction potentials

The total interaction energy U_{tot} can be separated into three contributions,

$$U_{\text{tot}} = U_{\text{mem}} + U_{\text{gg}} + U_{\text{nc}}, \tag{S9}$$

where U_{mem} represents the interaction energy between the membrane beads, U_{gg} accounts for the interaction of between subunits as well as with the membrane, and U_{nc} represents the interaction energy of the NC with the subunits and the membrane.

1. Membrane interactions

The membrane lipids consist of three beads, the first representing the lipid head and the other two connected through two finite extensible nonlinear elastic (FENE) bonds with maximum length $r_{\text{cut}} = 1.5\sigma$,

$$U_{\text{bond}}(r) = -\frac{1}{2} k_{\text{bond}} r_{\text{cut}}^2 \log \left[1 - (r/r_{\text{cut}})^2 \right]. \tag{S10}$$

with $k_{\text{bond}} = 30\epsilon_0/\sigma^2$. A harmonic spring links the two outer beads, to ensure that the lipids maintain a cylindrical shape,

$$U_{\text{bend}}(r) = \frac{1}{2} k_{\text{bend}} (r - 4\sigma)^2. \tag{S11}$$

All membrane beads interact via a Weeks-Chandler-Andersen potential,

$$U_{\text{rep}}(r) = \sum 4\epsilon_{\text{rep}} \left[\left(\frac{b_{i,j}}{r} \right)^{12} - \left(\frac{b_{i,j}}{r} \right)^6 + \frac{1}{4} \right], \tag{S12}$$

with $\epsilon_{\text{rep}} = 1$ and cutoff $r_{\text{cut}} = 2^{1/6} b_{i,j}$. The parameter $b_{i,j}$ depends on the identities of the interacting beads: $b_{\text{h,h}} = b_{\text{h,t}} = 0.95\sigma$ and $b_{\text{t,t}} = 1.0\sigma$, with the subscripts 'h' and 't' denoting head and tail beads, respectively. The hydrophobic nature of the lipid tails is accounted for by an attractive interaction between all pairs of tail beads:

$$U_{\text{hydro}}(r) = \begin{cases} -\epsilon_0, & r < r_{\text{c}} \\ -\epsilon_0 \cos \left[\pi(r - r_{\text{c}})/2\omega_{\text{c}} \right], & r_{\text{c}} \leq r \leq r_{\text{c}} + \omega_{\text{c}} \\ 0, & r > r_{\text{c}} + \omega_{\text{c}} \end{cases} \tag{S13}$$

with $\epsilon_0 = 1.0$, $r_{\text{c}} = 2^{1/6}\sigma$. The potential width ω_{c} is a control parameter that determines, among other properties, the membrane rigidity. Unless otherwise specified, $\omega_{\text{c}} = 1.6$.

2. GP-GP interactions

The interaction potential between GP subunits, U_{gg}, consists of two terms. The attractive interaction between a pair of attractor pseudoatoms 'A' of the active subunits is modeled by a Morse potential. Beads interact only with those of the same kind on a neighboring cone, A_i-A_i, $i = 2, .., 5$, and the equilibrium distance of the potential depends on the pseudoatom radius, r_i^{eq}:

$$U_{\text{gg}}^M = \sum_{i=2}^{5} U_i^M = \sum_{i=2}^{5} \epsilon_{\text{gg}} (e^{-2\alpha_i(r - 2r_i^{\text{eq}})} - 2e^{-\alpha_i(r - 2r_i^{\text{eq}})}) \tag{S14}$$

with $\alpha_i = (3.0/r_i^{\text{eq}})$. The cutoff of this interaction was set at $r_{\text{cut}} = 2r_i^{eq} + 3.5$. The subunit beads also experience excluded volume interactions,

$$U_{\text{g-g}}^{\text{ex}}(r) = \sum_i \sum_j 4\epsilon_{\text{ex}} \left[\left(\frac{b_{i,j}}{r} \right)^{12} - \left(\frac{b_{i,j}}{r} \right)^6 \right] \tag{S15}$$

with $\epsilon_{\text{ex}} = 1.0$ and cutoff radius $r_{\text{cut}} = b_{ij} = r_i^{\text{eq}} + r_j^{\text{eq}}$. The sum extends to all the subunit beads, both active and inactive.

In the subunits, only the pseudoatoms 'VX' interact with the membrane beads; there is no interaction between membrane beads and 'A' or 'B' pseudoatoms. The interaction between subunit excluders and membrane beads corresponds to the repulsive part of the Lennard-Jones potential,

$$U_{\text{g-m}}^{\text{ex}}(r) = \sum_i \sum_j 4\epsilon_{\text{ex}} \left[\left(\frac{b_{i,j}^{\text{g-m}}}{r} \right)^{12} - \left(\frac{b_{i,j}^{\text{g-m}}}{r} \right)^{6} \right], \tag{S16}$$

where i runs over all lipid beads and j over all 'VX' pseudoatoms, and $b_{i,j}^{\text{g-m}} = 0.5 + r_{\text{in}}$ for the inner excluders VX_{in} and $b_{i,j} = 0.5 + r_{\text{in}}$ for the outer excluders VX_{out}.

3. NC interactions

The NC beads interact with pseudoatoms A_3 of the active GP subunits through a Morse potential,

$$U_{\text{gg}}^{\text{M}}(r) = \sum_{\text{nc},j} \sum_{A_3} \epsilon_{\text{ng}} (e^{-2\alpha_{\text{nc}}(r - 2r_{\text{nc}}^{\text{eq}})} - 2e^{-\alpha_{\text{nc}}(r - 2r_{\text{nc}}^{\text{eq}})}) \tag{S17}$$

with $r_{\text{nc}}^{\text{eq}} = 1.0$ and $\alpha_{\text{nc}} = 2.5$. We explored a broad range of $\alpha_{nc} = 1.5 - 6.0$ and observed little difference in the morphology of the assembly product.

NC beads interact with all the membrane beads through a repulsive Lennard-Jones potential,

$$U_{\text{nc-m}}^{\text{ex}}(r) = \sum_i \sum_j 4\epsilon_{\text{ex}} \left[\left(\frac{b_{i,j}^{\text{nc-m}}}{r} \right)^{12} - \left(\frac{b_{i,j}^{\text{nc-m}}}{r} \right)^{6} \right], \tag{S18}$$

where i runs over all lipid beads and j over all NC pseudoatoms, and $r_{\text{cut}} = b_{i,j}^{\text{nc-m}} = 1.0$. Similarly, there is a a repulsive Lennard-Jones potential between NC pseudoatoms and certain GP pseudoatoms

$$U_{\text{nc-g}}^{\text{ex}}(r) = \sum_i \sum_j 4\epsilon_{\text{ex}} \left[\left(\frac{b_{i,j}^{\text{nc-g}}}{r} \right)^{12} - \left(\frac{b_{i,j}^{\text{nc-g}}}{r} \right)^{6} \right], \tag{S19}$$

where i runs over all NC beads and j over all the subunit pseudoatoms of the type A_4, A_5, B_6 and VX_{out}. We set the distance $b_{ij}^{\text{nc-g}} = 0.5 + r_i^{\text{eq}}$, with 0.5 the radius of the NC beads.

H. Relationship between subunit geometry and membrane reshaping

Subunit geometry. The geometry of the model GP trimer subunit used in the main text is schematically shown in Fig. S1. As explained in the main text, the subunit consists of three cones symmetrically placed around the subunit axis. Each cone contains six pseudoatoms. Only the inner four pseudoatoms (denoted as A) experience attractive interactions. The outer two pseudoatoms, B, interact with the rest through excluded volume. The pseudoatoms are placed at heights $h_i = [16.0, 17.5, 19.0, 20.5, 22.0, 23.5]\sigma$. At each plane $z = h_i$ there are three identical pseudoatoms forming an equilateral triangle of radius $l_i = h_i \tan \alpha_l$, where α_l can be tuned. Since assembly in bulk is slightly more robust for smaller α_l, we choose an optimal value $\alpha_l = 7°$. The radius of each pseudoatom is then given by $r_i^{\text{eq}} = l_i \cos \psi$, being ψ the parameter that controls the preferred curvature of the subunits. We set $\psi = 94.9°$ (see section S5). Finally, to embed the subunits in the membrane we add two layers of three membrane excluders ' VX ', consistent with the cone geometry, at height $h_{\text{in}} = 19.0\sigma$ (inner domain) and $h_{\text{out}} = 26.0\sigma$ (outer domain). The sequence of pseudoatoms across the shell reads [B_1,A_2,A_3,VX_{in},A_4,A_5,B_6,VX_{out}].

Effect of changing the subunit geometry. In our initial model for GP subunits, the cones were positioned entirely within the membrane, such that all lateral interactions between neighboring cones were within the body of the membrane (Fig. S2). Specifically, the membrane excluders were located at the same positions as the pseudoatoms B_1 and B_6. However, this subunit structure led to the formation of short budding necks around partial GP shells. The high curvature within such necks presented an extremely large barrier to subunit diffusion, and hence prohibited complete assembly and budding.

We explored several other subunit geometries. We found that displacing the cone attractor beads further to the outside of the membrane leads to similar results. However, when the cone pseudoatoms are displaced towards the interior of the shell, so that
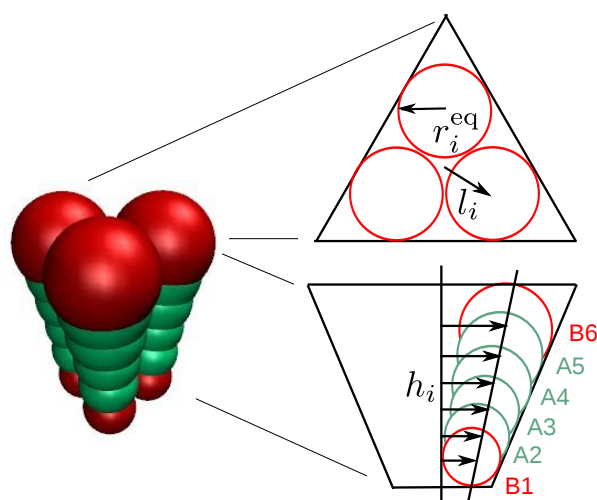
FIG. S1. Schematic of the subunit geometry, with views from directly above the plane of the membrane and within the plane of the membrane. Membrane excluders are not shown in these schematics to aid visual clarity.

the lateral interactions take place below the membrane, a longer neck with more shallow curvature forms. The reduced neck curvature lowers the barrier to subunit diffusion, allowing complete assembly and budding. The difference in neck geometry likely arises because the lower position of the subunit attractions allows them to exert a higher torque on the membrane. We note that this particular aspect of our subunit geometry does not conform to the actual GP structure and interactions; the lateral attractions between Sindbis GPs are primarily situated above the membrane. However, the neck geometry in these simulations (long and with shallow curvature) closely resembles those observed in experiments of in vivo virus assembly.
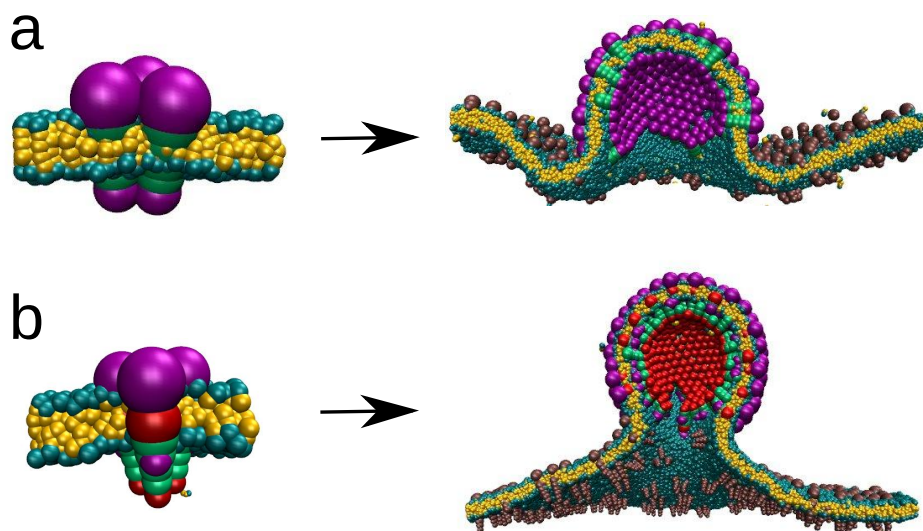

FIG. S2. Relationship between the structure of glycoproteins and their ability to reshape the membrane. **(a)** When 'A' pseudoatoms overlap with the membrane and the membrane excluders overlap with 'B' pseudoatoms, the budding neck develops acute angles around a partially assembled shell. This leads to a large barrier to subunit diffusion that prevents complete assembly and budding. **(b)** When both 'A' and 'B' pseudoatoms are situated below the membrane, the budding neck is longer, with a shallower angle. This reduces the barrier to subunit diffusion, allowing completion of assembly and budding.

S4.   ASSEMBLY AND BUDDING WITHOUT CONFORMATIONAL SWITCHING

Fig. S3 compares the fraction of trajectories leading to complete GPNC particles with and without conformational switching as a function of the GP-GP interaction strength. We see that, in the absence of conformational switching, complete assembly and budding only occurs in the limit of weak GP-GP interactions and a strong GP-NC interaction. Stronger GP-GP interactions allow nucleation of GP shells away from the vicinity of the nucleocapsid, thus leading to a kinetic trap in which too many shells have nucleated (Fig. S3b). Moderate GP-GP interactions avoid this trap, leading to assembly and budding of well-formed shells in about half of simulated trajectories. However, when the GP-GP interaction is further decreased, the assembly trajectory is dominated by the NC interaction. The GP subunits adsorb onto the NC without forming a well-defined lattice, leading to defective particles with holes. An example of such a configuration is shown within the plot.
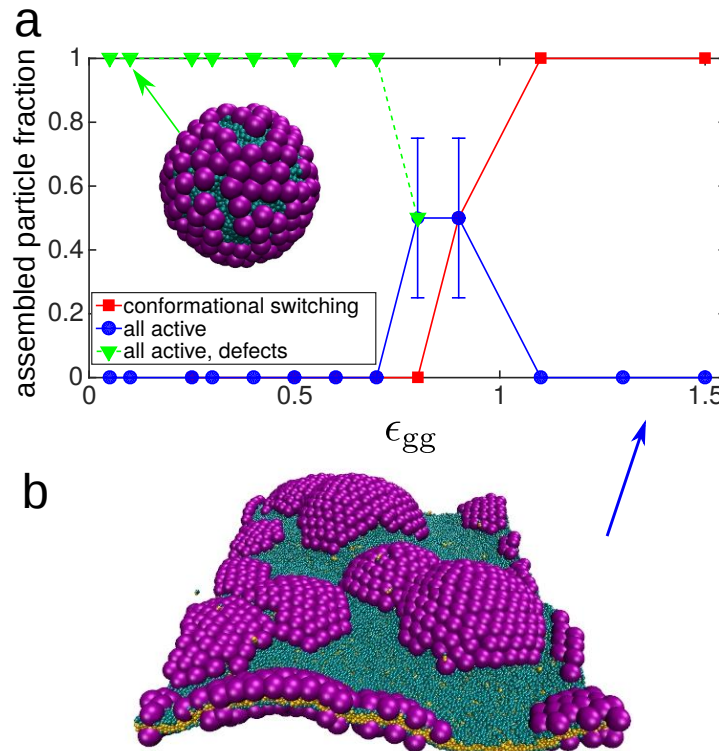

FIG. S3.   Effect of conformational switching (CS) on assembly and budding around a nucleocapsid. **a** Fraction of trajectories in which a complete shell assembled as a function of the GP-GP interaction strength, with constant $\epsilon_{ng} = 3.5$. Results are shown for simulations in which all the subunits are active ('all active', ●) and simulations with conformational switching ('conformational switching', ■). The fraction of trajectories leading to shells with large holes is shown for the case with conformational switching ('all active, defects', ▼). Each data point corresponds to 4 independent simulations. **b** Snapshot showing a typical, kinetically trapped configuration from a simulation without conformational switching with $\epsilon_{gg} = 1.3$.

S5.   BULK SIMULATIONS

The preferred curvature of the GP shell can be tuned by varying the cone angle ψ, which leads to aggregates of different shapes and sizes. To determine the relationship between cone angle and aggregate size, we performed bulk simulations (i.e. without a membrane present) of GP assembly. In these simulations we initialized 200 subunits with random positions and orientations (except not overlapping) in a box of size $180^3\sigma^3$. The subunit interaction was set at $\epsilon_{gg} = 0.995$, which allows assembly with high yield as shown in Fig. S4a. We find that for the cone angle $\psi = 94.9°$ the predominant assembled shell is roughly spherical and contains 80 subunits. The distribution of assembly products is shown in Fig. S4b for 19 simulations.

Although the subunit geometry locally favors hexagonal packing, formation of a closed capsid requires 12 five-fold defects [30]. We find that the spatial distribution of these defects is typically not fully consistent with icosahedral symmetry for dynamically formed capsids. We speculate that asymmetric model trimer subunits would be required to reliably obtain symmetric

T=4 structures. This is consistent with the equilibrium simulations in [31], which did not obtain T=4 structures for any enforced curvature, while curvatures consistent with T=3 and T=7 geometries did result in T=3 and T=7 structures. Wagner and Zandi [32] also found that T=4 structures were low probability outcomes of their nonequilibrium assembly algorithm. However, the relatively high monodispersity observed in our simulations suggests that the 80-subunit capsid is a free energy minimum and assembly is robust at these conditions.

We also performed bulk simulations examining GP assembly around a NC. These simulations were the same as described in the previous paragraph, except that the simulation box included one NC particle. We performed simulations over a range of NC radii to determine the optimal size for assembly of the GP shell, which identified an optimal NC radius of $r_{\mathrm{NC}} = 19.0\sigma$. This value is consistent with the position of the contact between the GP and the NC in Sindbis virus, ~ 19.5nm [11]. The distribution of end-products for bulk simulations at this NC radius are shown in Fig. S4b.
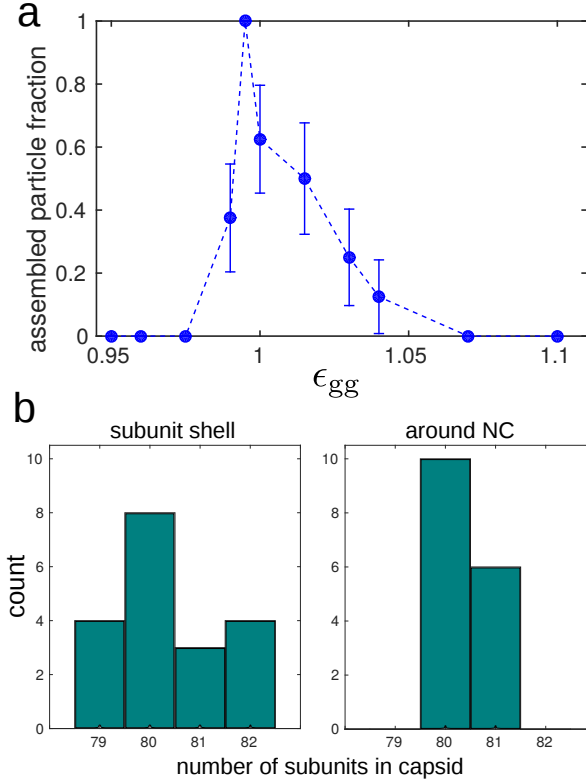

FIG. S4. **(a)** Fraction of trajectories that lead to assembled particles as a function of subunit interaction ϵ_{gg}, for 8 independent simulations. Parameters are: 200 GP subunits in a box with side length 180σ, with each simulation performed for $8.75 \times 10^5 \tau_0$. **(b)** Distribution of assembly products in bulk simulations (*i.e.* in the absence of the membrane). *(Left)* Assembly of GP subunits without a NC. *(Right)* Assembly around a spherical NC. In both cases $\epsilon_{\mathrm{gg}} = 0.995$, and for assembly around a NC $\epsilon_{\mathrm{ng}} = 1.8$. Each distribution is calculated from 19 independent simulations.

S6. SHELL AND MEMBRANE BENDING MODULUS ESTIMATION

A. Shell bending modulus

Our estimation of the shell bending modulus is based on the work on triangulated surfaces by Gompper and Kroll [33]. The discretization of the curvature in terms of the squared difference of the normal vector of neighboring subunits allows to express the discrete Helfrich bending energy as

$$H_{\mathrm{B}} = \frac{k}{2} \sum_{\alpha,\beta} (\hat{n}_\alpha - \hat{n}_\beta)^2 \equiv k \sum_{\alpha,\beta} (1 - \hat{n}_\alpha \cdot \hat{n}_\beta), \tag{S20}$$

with $k = \sqrt{3}\kappa$ and κ as the bending modulus. $\hat{n}_\alpha$ represents the normal vector to the subunit α, so that the angle θ between two adjacent subunits is given by $\hat{n}_\alpha \cdot \hat{n}_\beta = \cos\theta$. The energy can be rewriten as

$$H_{\mathrm{B}} = k \sum_{\alpha,\beta} [1 - \cos(\theta - \theta_0)], \tag{S21}$$

where θ_0 corresponds to the preferred curvature of the lattice, and the sum runs over all the subunit pairs interacting in the shell. Assuming small variations around the preferred angle results in

$$H_{\mathrm{B}} \approx \frac{k}{2} \sum_{\alpha,\beta} (\theta - \theta_0)^2. \tag{S22}$$

Therefore, if the interaction energy U_{gg} between subunits can be expressed as a function of the angle θ, comparison with (S22) allows to estimate the bending rigidty in terms of the parameters that define the interaction. As opposed to the two-dimensional case of triangulated surfaces, our subunits are three dimensional structures of finite thickness. The interaction between subunits is given by the Morse potential between 'A' pseudoatoms,

$$U_{\mathrm{gg}}^M = \sum_i U_i^{\mathrm{M}}(r_i), \tag{S23}$$

where r_i is the distance between pseudoatoms of the same type, and the index i runs over the four pseudoatoms $\{A_i\}$. In equilibrium, the angle between subunits is given by θ_0. But if the shell is subject to mechanical perturbations, the subunits will tilt around the neutral surface with an angle θ. For small perturbations, the potential (S23) is approximated by

$$U_{\mathrm{gg}}^{\mathrm{M}} \approx \frac{1}{2} \left. \frac{\partial^2 U_{\mathrm{gg}}^{\mathrm{M}}}{\partial \theta^2} \right|_{\theta=\theta_0} (\theta - \theta_0)^2. \tag{S24}$$
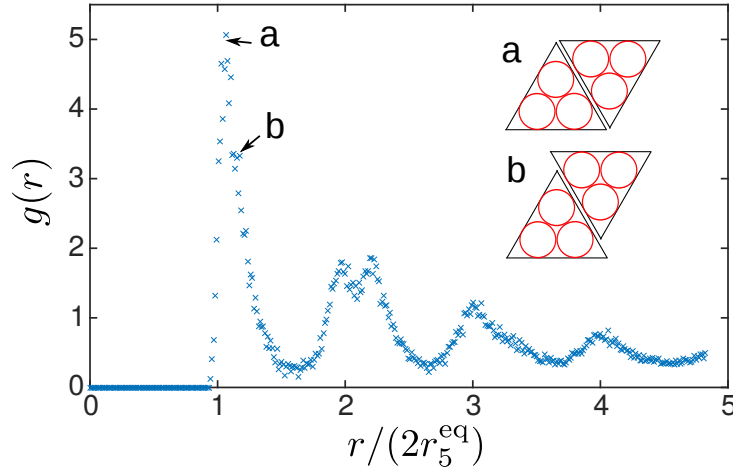

FIG. S5. Pair correlation function $g(r)$ for cone positions within assembled GP shells. To compute $g(r)$ we measure separations between pairs of A_5 pseudoatoms. In the plot we have scaled the separation r by the equilibrium distance of the Morse potential. The correlation function suggests that two possible configurations are present in the shell. In the configuration **a**, the nearest neighbor is located at a distance $r_{\mathbf{a}} = 2r_5^{\mathrm{eq}}$, whereas in configuration **b** it is found at $r_{\mathbf{b}} = \sqrt{3l_5^2/4 + (2r_5^{\mathrm{eq}})^2} \approx 1.16 r_{\mathbf{a}}$.

To determine the equilibrium positions of the subunits in the shell, we need to assess how they organize in the shell. Although the resulting structures are not perfectly ordered and there is some variation in the distribution of subunits, analysis of the pair correlation function $g(r)$, shown in Fig. S5, suggests that subunits organize into two configurations. We assume that the configuration in which the cones are separated by the equilibrium distance of the Morse potential, Fig. S5a, is dominant. In this configuration, the angle that minimizes the interaction energy U_{gg} is the angle that minimizes separately each term of (S23). By comparing expressions (S22) and (S24), the shell bending modulus can be expressed as

$$\kappa_{\text{shell}} = \frac{1}{\sqrt{3}} \sum_{\alpha,\beta} \sum_i \frac{\partial^2 U_i^{\text{M}}}{\partial^2 \theta} \bigg|_{\theta=\theta_0}, \tag{S25}$$

A more detailed explanation of the interaction is given in Fig. S6. In this configuration, the pseudoatoms in cone 'a' in the subunit α interact with pseudoatoms in cones 'b' and 'c' in subunit β and the analogous pseudoatoms in subunit γ. Taking into account the symmetry of the system, we only consider the interaction of the cone 'a' with cones 'b' and 'c'. Pseudoatoms A_i in cones 'a' and 'b' are separated by a distance $r_i^{\text{ab}} = 2r_i^{\text{eq}}$. Pseudoatoms 'a' and 'c' are however separated by a much larger distance, $r_i^{ac} = \sqrt{(r_i^{\text{ab}})^2 + 3l_i^2}$. Hence we only consider interactions between nearest neighbors and neglect second-neighbors.

The Morse potential explicitly depends on the distance between pseudoatoms, so in practice one needs to express this distance in terms of the angle, $r_i = r_i(\theta)$, and thus the previous expression reads

$$\kappa_{\text{shell}} = \frac{1}{\sqrt{3}} \sum_{\alpha,\beta} \sum_i \frac{\partial^2 U_i^{\text{M}}}{\partial r_i^2} \left(\frac{\partial r_i}{\partial \theta}\right)^2 \bigg|_{\theta=\theta_0}, \tag{S26}$$

where the second derivative of the Morse potential yields

$$\frac{\partial^2 U_i^{\text{M}}}{\partial r^2} \bigg|_{r=2r_i^{\text{eq}}} = 2\epsilon_{\text{gg}} \alpha_i^2, \tag{S27}$$

Considering the symmetry of the system, we can compute the total interaction as $3n_i/2$ the interaction between a pair of cones, where 3 corresponds to the number of cones per subunit and n_i is the average number of interacting neighbor cones. Consistent with hexagonal packing, we set $n_i = 4$ (since two neighbor cones are in the same rigid body).

The neutral surface of the interaction between subunits corresponds to the position at which the stress between the subunits vanish, given by the condition $dU_{\text{gg}}^{\text{M}}/dx = 0$ along the midsurface between both subunits. We calculated the position of the neutral surface h_n numerically, and found a position close to central point of the cones, situated between pseudoatoms A_3 and A_4. For simplicity, we take $h_{\text{n}} = (h_3 + h_4)/2$.

To obtain the distance between the pseudoatoms in cones 'a' and 'b' with respect to variations in the angle between subunits when they rotate with respect to the neutral surface, we initialize the subunits centered at the neutral surface position. Following the scheme shown in Fig. S6 the coordinates of the pseudoatoms in cone 'a' and 'b' are initially given by

$$\vec{a}_i = [l_i/2, \sqrt{3}l_i/2, \bar{h}_i], \tag{S28}$$
$$\vec{b}_i = [-l_i/2, \sqrt{3}l_i/2, \bar{h}_i], \tag{S29}$$

where we have introduced $\bar{h}_i = h_i - h_{\text{n}}$. The subunits are rotated by an angle $\theta/2$ in the case of 'a' and by $-\theta/2$ in 'b'. Subunits α and β are then translated by a distance $-d_{\text{n}}/2$ and $+d_{\text{n}}/2$, respectively, along the direction $\hat{x}$, with d_{n} as the equilibrium distance between subunits at a height h_{n}.

$$\vec{a}_i \rightarrow \hat{\mathcal{R}}_y(\theta/2)\vec{a}_i - d_n/2\hat{x}. \tag{S30}$$
$$\vec{b}_i \rightarrow \hat{\mathcal{R}}_y(-\theta/2)\vec{a}_i + d_n/2\hat{x}. \tag{S31}$$

Finally, the distance between pseudoatoms a_i and b_i reads

$$r_i^{\text{ab}}(\theta) = 2\bar{h}_i \sin(\theta/2) - l_i \cos(\theta/2) + d_{\text{n}}. \tag{S32}$$

As suggested by analysis of Fig. S5, in the shell the distance between atoms is given by the equilibrium distance of the Morse potential, $2r_i^{\text{eq}}$. Taking $r_i^{\text{ab}} = 2r_i^{\text{eq}}$, this set of equations allows to evaluate the equilibrium angle θ_0 and distance between the subunits d_{n}, obtaining $\theta_0 = 18.6°$ and $d_{\text{n}} = 7.36\sigma$. Computing the derivative of expression (S32) and inserting the result in (S26), the shell bending rigidity is obtained as a function of the Morse potential depth ϵ_{gg}, obtaining

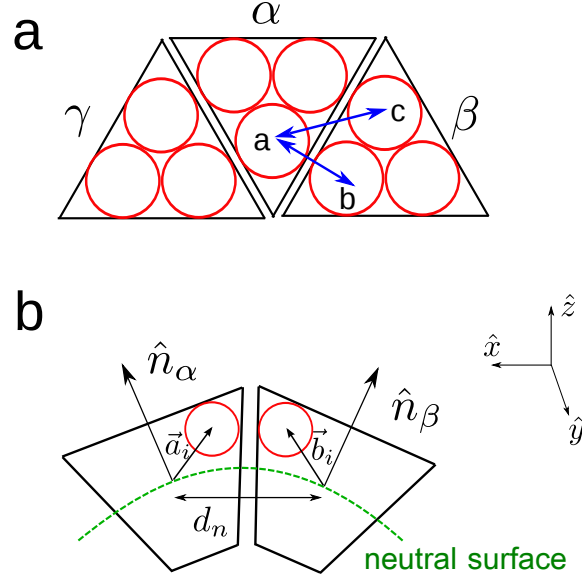$$\kappa_{\text{shell}} \approx 25.66\epsilon_{\text{gg}}. \tag{S33}$$

FIG. S6. Subunit organization in the shell. **a)** Top view showing the outermost attractive beads in each subunit. For the purpose of estimating the elastic properties of the shell, we consider that all the subunits are organized in such a way that each pseudoatom interacts with two of the pseudoatoms of the neighboring subunits as indicated. **b)** Lateral view of the subunits in the shell, with the vector positions $\vec{a}_i$ and $\vec{b}_i$ indicated. The location of the neutral surface is shown by the green dashed line, and $\hat{n}_\alpha$ and $\hat{n}_\beta$ represent the subunit normal vectors.

B. Membrane bending modulus

The membrane bending modulus is estimated from the height-height fluctuation spectrum. We analyze the fluctuations of a free membrane (*i.e.* without embedded subunits) of size $170\text{x}170\sigma^2$. After equilibrating the membrane during $1,500\tau_0$, we measure the membrane position for 200 configurations separated by $75\tau_0$. The membrane height $h(\mathbf{x})$ is evaluated from the tail bead positions, and mapped onto a 57x57 grid. Following a standard procedure [12, 34] the undulation modes in real space can be decomposed in modes in Fourier space,

$$h(\mathbf{x}) = \sum_{\mathbf{q}} h(\mathbf{q})e^{i\mathbf{q}\cdot\mathbf{x}}. \tag{S34}$$

where $\mathbf{q} = (q_x, q_y) = (n,m)2\pi/L$. From the equipartition theorem, the fluctuation spectrum reads

$$\langle|h(q)|^2\rangle = \frac{k_{\mathrm{B}}T}{L^2\left[\kappa q^4 + \gamma q^2\right]}, \tag{S35}$$

where γ is the remnant surface tension of the membrane. Even for very small surface tension, in the smaller wave modes the fluctuation spectrum is dominated by tension. For the the analysis we only consider the modes $2\pi/q > 5d$, where d is the membrane thickness. Fig. S7a shows an example of the fluctuation spectrum for a membrane at $\omega_{\mathrm{c}} = 1.6$, with ω_{c} the width of the attractive potential between lipid tail beads (Eq. S13). The results are fit to a q^{-4} curve, obtaining the bending rigidity. Fig. S7b shows our estimation of the membrane bending modulus as a function of the control parameter ω_{c}. Note that at high $\omega_{\mathrm{c}} > 1.65$ our results suggest a slightly lower bending modulus than that obtained by Cooke *et al.* [12].

S7. SUBUNIT AND LIPID DIFFUSION IN THE MEMBRANE

We estimate the subunit diffusion constant in the membrane from the subunit mean square displacement versus time [35],

$$\langle|\mathbf{r}_\parallel(t) - \mathbf{r}_\parallel(0)|^2\rangle = 4Dt. \tag{S36}$$

We equilibrate a membrane of size $50\text{x}50\sigma^2$ during $1{,}500\tau_0$, and then sample during $75\tau_0$ with period $0.15\tau_0$. Averaging over 20 independent simulations of a single subunit diffusing on membrane, we obtain a subunit diffusion constant $D_{\text{sub}} = 1.0\sigma^2/\tau_0$. A similar value is obtained at the subunit concentration used in our simulations (membrane fraction covered by subunits ≈ 0.15), meaning that we have not reached the limit of protein crowding in which diffusion decreases [35]. Using the same method for the lipids, and averaging over 500 molecules, we obtain $D_{\text{lip}} = 0.12\sigma^2/\tau_0$. The fact that subunits diffuse faster than lipids might be expected, since the subunit pseudoatoms which overlap with the membrane do not interact with the lipids, whereas lipids are subject to much higher friction as they interact with all the neighboring lipids. In biological membranes, however, transmembrane proteins usually diffuse around 3-4 times slower than lipids. This unrealistic fast diffusion was intentionally introduced in the model to speed up the simulation, allowing assembly completion within a tractable simulation time. The characteristic timescale of our simulation is then given by the subunit diffusion, as explained in the main text.
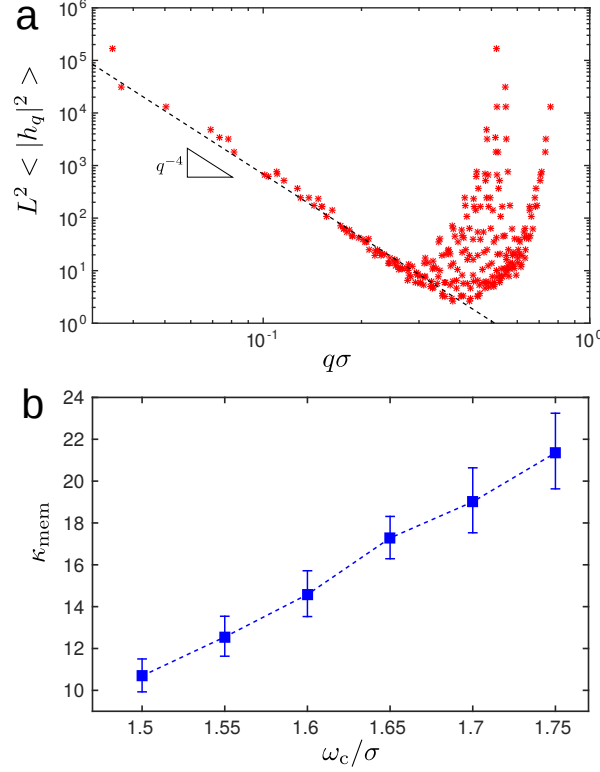

FIG. S7. **a)** Fluctuation spectrum $< |h(\mathbf{q})|^2 >$ as a function of the wave mode q, for $\omega_{\text{c}} = 1.6$. The dashed line represents the fit curve q^{-4}. **b)** Membrane bending modulus κ_{mem} measured from the fluctuation spectrum as a function of the parameter ω_{c}.

S8. ADDITIONAL FIGURES

The relative contributions from GP-GP and GP-NC interactions are compared in Fig. S8, and the distributions of assembly outcomes for representative values of ϵ_{gg} are shown in Fig. S9.
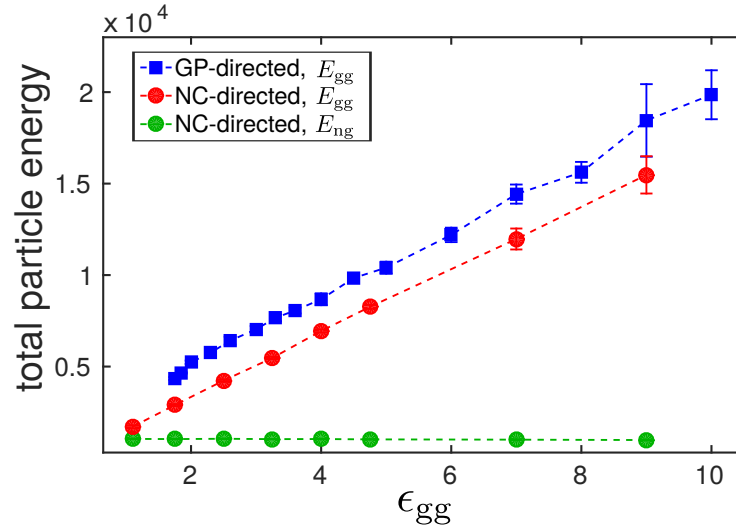
FIG. S8.   Total particle energy, accounting for the attractive energy of the Morse potentials of all the pseudoatoms that form the particle, as a function of the subunit interaction ϵ_{gg}. Results are shown for a GP-particle (■ symbols) and a GPNC-particle with $\epsilon_{ng} = 3.5$. For the GPNC-particle, the energy is separated into the components arising from GP-GP interactions (E_{gg}, ● symbols) and from GP-NC interactions (E_{ng}, ● symbols).
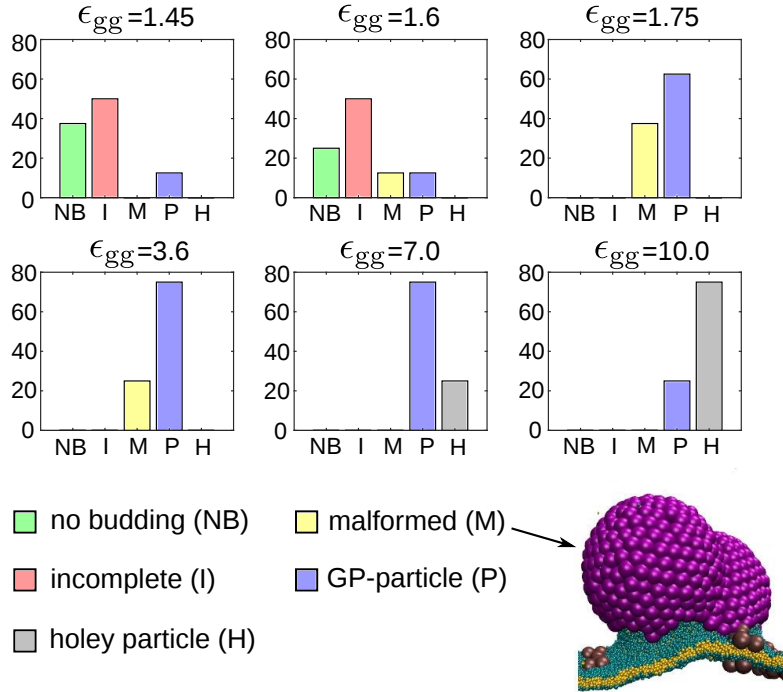

FIG. S9. Probability of each assembly outcome for some representative values of ϵ_{gg} in GP-directed budding. We find no parameter value for which malformed capsids (for which a typical example is shown) are predominant, but they represent up to 40% of the simulation outcomes at $\epsilon_{gg} = 1.75$.

[1] S. Safran, *Statistical Thermodynamics of Surfaces, Interfaces, and Membranes* (Addison-Wesley Pub., 1994).

[2] M. F. Hagan, Adv. Chem. Phys. **155**, 1 (2014).

[3] A. A. Waheed and E. O. Freed, Viruses **2**, 1146 (2010).

[4] S. Welsch, B. Müller, and H.-G. Kräusslich, FEBS Lett. **581**, 2089 (2007).

[5] J. S. Rossman and R. A. Lamb, Virology **411**, 229 (2011).

[6] T. Ruiz-Herrero and M. F. Hagan, Biophys. J. , 1 (2015).

[7] R. P. Bradley and R. Radhakrishnan, Proc. Nat. Acad. Sci. USA **113**, 5117 (2016).

[8] M. Deserno, Chemistry and Physics of Lipids **185**, 11 (2015), membrane mechanochemistry: From the molecular to the cellular scale.

[9] Helfrich, W., J. Phys. France **47**, 321 (1986).

[10] S. Mukhopadhyay, W. Zhang, S. Gabler, P. R. Chipman, E. G. Strauss, J. H. Strauss, T. S. Baker, R. J. Kuhn, and M. G. Rossmann, Structure **14**, 63 (2006).

[11] W. Zhang, S. Mukhopadhyay, S. V. Pletnev, T. S. Baker, R. J. Kuhn, and M. G. Rossmann, Journal of Virology **76**, 11645 (2002).

[12] I. R. Cooke, K. Kremer, and M. Deserno, Phys. Rev. E **72** (2005).

[13] T. R. Weikl, M. M. Kozlov, and W. Helfrich, Physical Review E **57**, 6988 (1998), pRE.

[14] S. Semrau, T. Idema, T. Schmidt, and C. Storm, Biophysical Journal **96**, 4906 (2009), times Cited: 36 Semrau, Stefan Idema, Timon Schmidt, Thomas Storm, Cornelis Schmidt, Thomas/B-6296-2009; Semrau, Stefan/B-9772-2009; Idema, Timon/I-6547-2012; Storm, Cornelis/K-1486-2013 Idema, Timon/0000-0002-8901-5342; Storm, Cornelis/0000-0002-4391-8984 36.

[15] B. J. Reynwar and M. Deserno, Soft Matter **7**, 8567 (2011).

[16] M. Goulian, R. Bruinsma, and P. Pincus, EPL (Europhysics Letters) **22**, 145 (1993).

[17] M. Deserno, Macromol. Rapid Commun. **30**, 752 (2009).

[18] J. Wang, V. Rayaprolu, S. Mukhopadhyay, and Z. A., ACS Nano **9**, 8898 (2015).

[19] I. A. T. Schaap, F. Eghiaian, A. des Georges, and C. Veigel, J. Biol. Chem. **287**, 41078 (2012).

[20] N. Kol, Y. Shi, M. Tsvitov, D. Barlam, R. Shneck, M. Kay, and I. Rousso, Biophys. J. **92**, 1777 (2007).

[21] C. Packianathan, S. P. Katen, C. E. Dann, and A. Zlotnick, J. Virol. **84**, 1607 (2010).

[22] L. Deshmukh, C. D. Schwieters, A. Grishaev, R. Ghirlando, J. L. Baber, and G. M. Clore, J. Am. Chem. Soc. **135**, 16133 (2013), pMID: 24066695, http://dx.doi.org/10.1021/ja406246z.

[23] A. Zlotnick and S. Mukhopadhyay, Trends Microbiol. **19**, 14 (2011).

[24] G. Lazaro and M. Hagan, J. Phys. Chem. B , 6306 (2016).

[25] J. M. A. Grime, J. F. Dama, B. K. Ganser-Pornillos, C. L. Woodward, G. J. Jensen, M. J. Yeager, and G. A. Voth, Nat. Comm. **in press** (2016).

[26] K. Forsell, L. Xing, T. Kozlovska, R. H. Cheng, and H. Garoff, EMBO Journal **19**, 5081 (2000).

[27] T. D. Nguyen, C. L. Phillips, J. A. Anderson, and S. C. Glotzer, Comput. Phys. Commun. **182**, 2307 (2011).

[28] R. Matthews and C. Likos, Phys. Rev. Lett. **109**, 178302 (2012).

[29] v. C. Bonsdorff and S. Harrison, J. Virol. **28**, 578 (1978).

[30] G. M. Grason, The Journal of Chemical Physics **145**, 110901 (2016), http://dx.doi.org/10.1063/1.4962629.

[31] T. Chen and S. C. Glotzer, Physical Review E. **75**, 051504 (2007).

[32] J. Wagner and R. Zandi, Biophys. J. **109**, 956 (2015).

[33] G. Gompper and D. Kroll, J. Phys. I France **6**, 1305 (1996).

[34] E. Brandt, A. Braun, J. N. Sachs, J. Nagle, and O. Edholm, Biophys. J. **100**, 2104 (2011).

[35] J. Goose and M. Sansom, PLoS Computational Biology **9**, e1003033 (2013).